

Emerging correlated charge orders in a layered super-atomic crystal

Shuya Xing^{1,+}, Linlu Wu^{1,+}, Zilu Wang^{1,+}, Xu Chen^{2, +}, Haining Liu^{3,4}, Shuo Han¹, Le Lei¹, Qi Zheng^{2,4}, Li Huang^{2,4}, Xiao Lin⁴, Liming Xie^{3,4}, Xiaolong Chen^{2,4,5} Hong-Jun Gao^{2,4}, Zhihai Cheng^{1,*}, Jiangang Guo^{2,5,*}, Shancai Wang^{1,*}, and Wei Ji^{1,*}

¹*Beijing Key Laboratory of Optoelectronic Functional Materials & Micro-nano Devices, Department of Physics, Renmin University of China, Beijing 100872, China*

²*Beijing National Laboratory for Condensed Matter Physics, Institute of Physics, Chinese Academy of Sciences, P.O. Box 603, Beijing 100190, China.*

³*CAS Key Laboratory of Standardization and Measurement for Nanotechnology, CAS Centre for Excellence in Nanoscience, National Centre for Nanoscience and Technology, Beijing 100190, China*

⁴*University of Chinese Academy of Sciences, Beijing 100039, China*

⁵*Songshan Lake Materials Laboratory, Dongguan, Guangdong 523808, China*

Abstract: Synthesis of emergent crystals is the foundation of discovering novel phenomena and exploring intriguing properties. Comparing to the diverse exotic quantum states of covalent crystals, the unique super-atomic crystals are far from being extensively investigated in the case of their versatile superatoms (building blocks) and inter-superatom coupling (non-covalent interactions). Here, we investigate the correlated electronic structures in the layered super-atomic crystal of $\text{AuTe}_2\text{Se}_{4/3}$ (ATS), which can be assumed as three-dimensional triclinic stacking of the cube super-atoms ($\text{Au}_6\text{Te}_{12}\text{Se}_8$, 0D) with the anisotropic covalent-like inter-cube $\text{Te}\dots\text{Te}$ bonds. The sequential-emerged anisotropic triple CDW charge modulation, antipolar charge orders and quasi-2D Fermi surface were discovered in ATS using scanning tunneling microscopy/spectroscopy (STM/STS) in combination with angle-resolved photoemission spectroscopy (ARPES), transport measurement and Raman spectra. DFT calculations disclose the emerging and correlation mechanism of CDW and antipolar charge orders via the unique layered super-atomic crystal geometry and electronic structures. This work not only provides an unprecedented microscopic picture of novel electronic phase in the ATS, but also suggests a new category of super-atom layered materials with manipulatable properties through their high and precise tunability of super-atomic units and inter-unit interactions.

⁺ These authors contributed equally: Shuya Xing, Linglu Wu, Zilu Wang, Xu Chen.

* Email: zhihaicheng@ruc.edu.cn jgguo@iphy.ac.cn scw@ruc.edu.cn wji@ruc.edu.cn

Introduction

Synthesis of emergent crystals is the foundation of discovering novel phenomena, exploring intriguing properties and uncovering previously unknown principles in research of, e.g. Iron-based superconductors ($\text{La}[\text{O}_{1-x}\text{F}_x]\text{FeAs}$)¹, perovskite solar cells ($\text{CH}_3\text{NH}_3\text{PbI}_3$ ² and $\text{CH}_3\text{NH}_3\text{PbBr}_3$ ³), two-dimensional magnetism (CrI_3)⁴⁻⁶ and among the others. However, it was inherently limited that subsequent optimization of those crystals, e.g. $\text{La}[\text{O}_{1-x}\text{F}_x]\text{FeAs}$, by altering one type of atoms with another). The limited number of 82 stable and non-radioactive elements aside, each of them has its intrinsic characteristics that governs which other atoms it could chemically bond to. Thus, substitution of a new type of atoms usually introduces different structures with largely varied properties, which poses an overwhelming challenge to rational design of functional materials.

Non-covalent, e.g. van der Waals (vdW), interactions seem a cure for this challenge. A typical two-dimensional (2D) few-layer is comprised of several dangling-bond-free monolayers formed with intralayer covalent bonds, stacking together through weaker vdW attractions. The stacking usually introduces interlayer wavefunction overlap with subsequent electronic hybridization, previously known as covalent-like quasi-bonding (CLQB) as the overlapped wavefunction yields a covalent-like charge redistribution characteristic at the interlayer region⁷⁻¹⁰. It offers a route to drastically change bandgaps, optical transitions, topological properties, magnetism, electrical polarization, superconductivity and among the others of 2D few-layers with much higher feasibility compared with traditional bulk crystals by stacking, twisting, bending and compressing.

In spite of huge success achieved in building novel 2D homo- and hetero-structures, covalent bonding still governs the in-plane position and type of atoms in each monolayer. An even aggressive strategy lies in introducing in-plane non-covalent bonding, namely, using atomic clusters, instead of atoms, as building blocks to construct layered materials through non-covalent bonding. Those atomic clusters are also known for super-atoms, which have, in principle, countless species available for materials design. Super-atomic crystals¹¹⁻¹³ could be assembled through inter-ligand or electrostatic interaction, molecular recognition or covalent

linkage among super-atoms, each of which usually results in a weak inter-super-atom electronic interaction. As an emergent linkage for super-atomic crystals, C \cdots C CLQB helps with forming free-electron-like bands in pentacene¹⁴ and C₆₀ monolayers¹⁵ under finely tuned compression being applied from vdW substrates. Nevertheless, weakly-coupled electronic interactions in those cases are apart from strong electron-electron or electron-quasiparticle interactions which are the origin of many intriguing and complicated physical phenomena¹⁶⁻¹⁹, e.g. charge density wave (CDW) and superconductivity, observed in quantum materials.

Here, we show experimental evidence for strong electronic interactions in a rationally designed layered crystal of high-symmetry, cubically shaped Au₆Te₁₂Se₈ (ATS)^{25,26} super-atomic crystal (Fig. 1), which offers up-to 12 Te \cdots Te CLQB and was found to be superconducting below \sim 2.8K. The Te \cdots Te quasi-bonding appears an enthralling non-covalent interaction in terms of small energy cost, high tunability and strong electronic coupling, as illustrated in layered Te allotropes.^{20,21} The surface electronic structures and electrical properties of ATS were revealed using low-temperature scanning tunneling microscope (LT-STM), angle-resolved photoemission spectroscopy (ARPES) together with Raman and transport measurements, and density functional theory calculations. We found two charge orders on the cleaving surface, namely a triple-cube-width stripe period along the *b*-axis and a spontaneous electric polarization with interlock anti-polar directions along the *a*-axis. The former exhibits a site-specific CDW gap of \sim 0.17 eV at 9 K, ascribed to a Fermi surface nesting effect while the latter is a result of inter-cube electronic hybridization reinforced by the CDW. The stripe order occurs below 120 K while the following anti-polar order becomes clearly visible below 100 K. Our results clearly demonstrated that super-atom layers could offer strong in-plane electronic coupling, which opens a category of layered materials for exhibiting manipulatable novel properties in tremendous layered structures with high and precise tunability.

Results and discussion

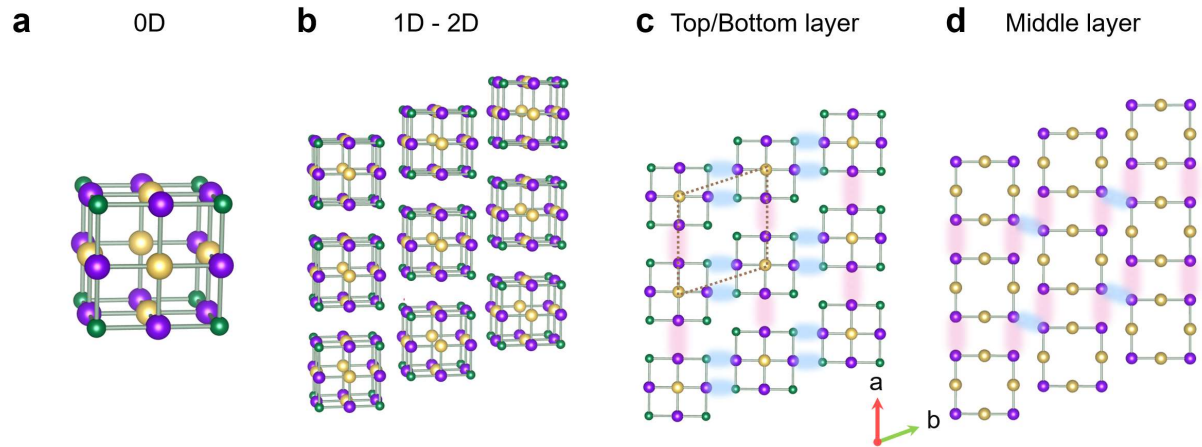


Figure 1. Atomic structure and the stripe charge order in the layered ATS supercrystal. **a**, The individual cube unit of ATS can be assumed as a supermolecule (0D). **b**, The atomically ordered ATS cubes form one-dimensional (1D) chains along the *a*-axis and the two-dimensional (2D) *ab*-plane layer through the inter-cube anisotropic interactions. **c**, **d**, The schematic models for the inter-cube Te \cdots Te bonding within the top/bottom cube layer (**c**) and the middle cube layer (**d**). Yellow, Au; Purple, Te; Green, Se.

Super-atomic crystal and CLQBs

An ATS super-atom is comprised of orderly arranged Au, Te and Se atoms showing a cube-like high-symmetric geometry, in which those three types of atoms are located at the faces, edges and corners, respectively (Fig. 1a). In its crystal, these cubes are stacked into one-dimensional (1D) chains along the *a*-axis which align together to form a 2D layer in the *ab*-plane (Fig. 1b and Supplementary Fig. 1). These layers are further stacked into a three-dimensional super-atomic crystal along the *c*-axis (Supplementary Fig. 2). In a layer of ATS, the lattice possibly reduces its symmetry, showing the P2 (P211) symmetry on the cleaving surface. These super-atoms are more flexibly to bond with each other, in comparison with traditional atoms, like Te, which allows to form complicated and highly tunable 2D Te \cdots Te quasi-bonding networks on the surface. In particular, there are four Te \cdots Te quasi-bonds (red shadowed lines and embedding green dotted lines in Fig. 1c and 1d), i.e. two in the top and bottom layers (Fig. 1c) and the other two in the middle layer (Fig. 1d), participating the formation of the chain. An additional quasi-bond (the red shadow and violet dotted lines in Fig. 1d) was found in the middle layer connecting two corner Te atoms across the chains, suggesting strong anisotropy of inter-cube interactions in the surface layer (Supplementary Fig. 3).

Two experimentally revealed charge orders

Figure 2a plots the measured temperature-dependent resistivity and its first-order derivative of an ATS thin-film sample. A nearly line relation was observed before the sample cooling down to 80 K where an abrupt change occurs, suggesting the emergence of a likely charge order. As the temperature further decreased, a superconducting transition characteristic appears at 2.8 K (Supplementary Fig. 4) [1]. The likely charge order transition at 80 K seems nonsynchronous with the geometrical transition, as indicated by a temperature-dependent Raman shift measurement (Fig. 2b). While Raman peak at 20 cm^{-1} (RP1) fades out during a cooling-down process of the sample, a new peak (RP2) emerges and gradually blue shifts. The position of RP2 eventually maintains at $\sim 205\text{ cm}^{-1}$ below 120 K. ~~The blue shift corresponds to the first order phase transition, which represent only a slight structural change of ATS.~~ It is thus of interest to uncover the reason why both macroscopic measurements reveal different transition temperatures.

Figure 2c-2f show a series of temperature-dependent STM images and their corresponding FFT patterns acquired at 80, 100, 120 and 150 K, respectively. The image acquired at 150 K (Fig. 2f) shows a chain-like appearance, which indicates no charge modulation, although the chain-like pattern confirms the expected anisotropic inter-cube interaction. A triple-chain-width, stripe-like charge modulation fades in at $\sim 120\text{ K}$ (Fig. 2e) and becomes clearer at $\sim 100\text{ K}$ (Fig. 2d). Aside from this, an additional order emerges along the a -axis when the temperature decreases to $\sim 80\text{ K}$, as reflected by the change of those FFT spots shown in the inset of Fig. 2c, which was more closely examined in a zoomed-in STM topographic image acquired at 9 K (Fig. 2g). The image indicates that the chain-like feature is parallel to the a -axis. Its corresponding FFT pattern confirms that the stripe width of three ATS chains (along the b -axis) that a characteristic peak ($q^* = b^*/3$) was observed in the b^* -axis where a^* and b^* are Bravais vectors of the reciprocal lattice of the ATS surface.

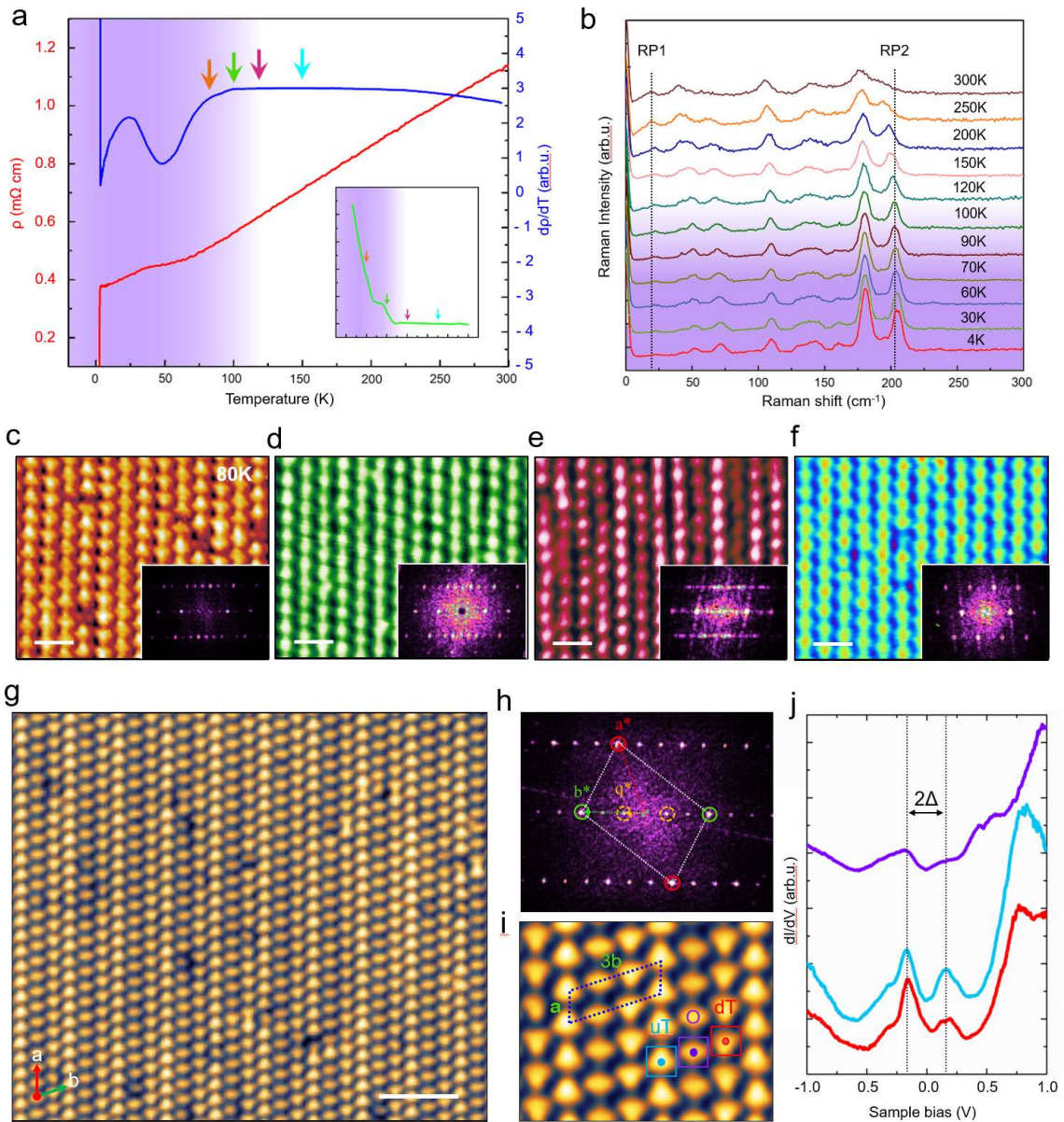


Figure 2. Triple CDW transition in the super-atomic crystal of ATS. **a**, Temperature-dependent resistivity (red) and its derivative (blue) curves around the triple CDW transition. The insert is the second order derivative (green) curves around the charge polarization transition. **b**, Temperature-dependent Raman spectrum. A new Raman peak emerged and gradually blue shifted with the decreased temperatures, and maintained at $\sim 205 \text{ cm}^{-1}$ below 120K. **c-f**, STM topography and the corresponding FFT patterns obtained at the temperature of 150K (**c**), 120K (**d**), 100K (**e**) and 80K (**f**), which are marked by the color-coded arrows in (**a**). **g**, Large-scale STM topography at 9K. **h**, The corresponding FFT of (**g**). The red and green circles mark the Bravais vectors (a^* and b^*) of the pristine ab -plane layer, respectively. The orange circles mark the Bravais vectors ($q^* = b^*/3$) of the triple stripe charge order. **i**, High-resolution STM image for the 1×3 supercell of the triple CDW. **j**, STS spectra of **A**, **B** and **B'** cube unit, showing a charge order gap of $\sim 0.17 \text{ eV}$. STM size and bias voltage: scale bar, 5nm, $V_s = +1.2 \text{ V}$ (**g**), scale bar, 2nm, $V_s = +1.2 \text{ V}$ (**h**).

A further zoomed-in image (Fig. 2i) depicts the additional order which represents sequential-emerged electrical polarization along the *a*-axis (Supplementary Fig. 5). Particularly, in each period of the stipe, three chains of ATS cubes show ``up-triangular'' (uT), ``olive-shaped'' (O) and ``down-triangular'' (dT) shapes in an occupied state STM image, respectively, while every cube in one chain shows the same appearance. The similarity of ATS cubes in each chain is also embodied in their spectroscopic features that their conductance spectra show inappreciable differences. However, this is not the case for different chains. Figure 2j shows the chain-specific conductance (dI/dV) spectra obtained on the uT, O and dT chains within one triple-chain stripe. All of them show a quasi-gap of ~ 0.17 eV around the Fermi level only observable below 150 K (Supplementary Fig. 7); this suggests the stripe order is of a charge density wave characteristic. The density of states (DOS) within the gap are not completely suppressed, in agreement with the metallicity of ATS. It is also noted that the quasi-gap in the uT or dT chains is more prominent than that in the O chain. A similar gap is also observed in our low temperature ARPES results, as elucidated later. In short, we experimentally found two charge orders, namely one CDW charge modulation along the *b*-axis and an electrical polarization showing charge redistribution within the high-symmetric ATS cube along the *a*-axis (Supplementary Fig. 6).

Origin of the CDW order

Density functional theory calculations were carried out to reveal the origin of the CDW order. A monolayer was used as a prototypic system as the CDW order was observed on the surface. Figure 3a illustrates the 2D Brillouin zone (BZ) of the monolayer, imposed with its real-space lattice vectors and an atomic model of ATS. Figure 3b depicts its Fermi surface (FS), which is highly anisotropic. A ribbon contains at least two bands developing in the $\Gamma - X$ direction, which embeds a small closed ellipse whose long axis is parallel to the $\Gamma - X$ direction, while a larger ellipse-shaped band is observable with its long axis perpendicular to the $\Gamma - X$ direction. The intersection point of the small ellipse and the $\Gamma - X$ path is close to 1/3 of $\Gamma - X$, consistent with the occurrence of FS nesting with a nesting vector of $(1/3, 0)$ in

the pristine monolayer ATS (Supplementary Fig. 8). This FS nesting could lead to the formation of the triple CDW along the *b*-axis due to the instability of Fermi surface, which is consistent with the triple feature of the observed stripe charge order in ATS.

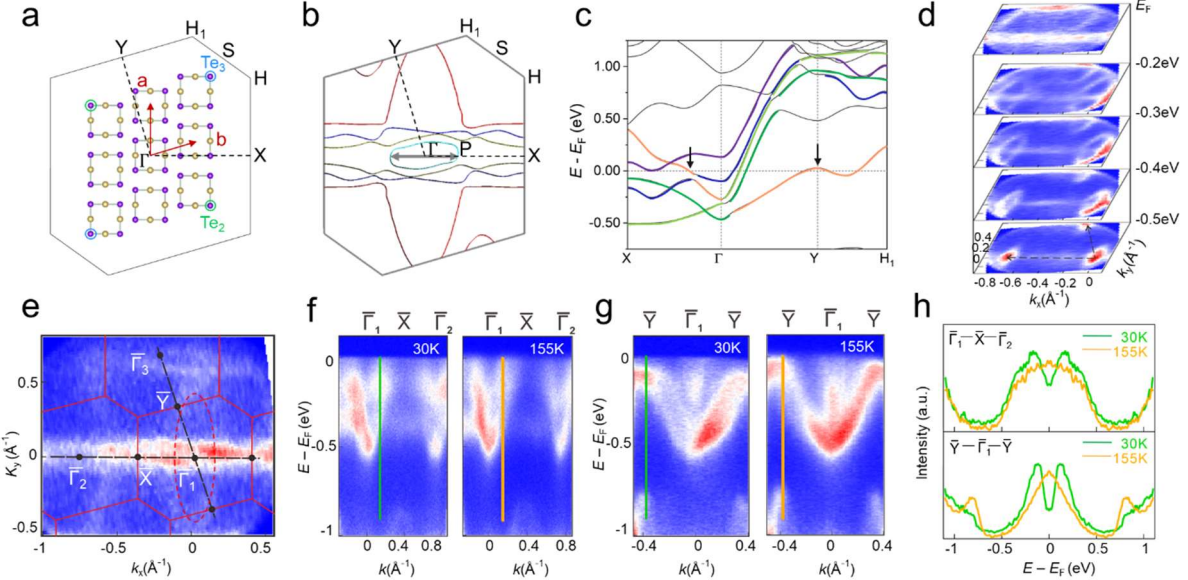


Figure 3. Electronic structure of the triple CDW of ATS. **a**, The 2D Brillouin zone (BZ) in *k*-space and the corresponding structural model in real space of the *ab*-plane. **b**, Calculated Fermi surface (FS) of the *ab*-plane monolayer with the four color-coded Fermi sheets. The intersection of the cyan Fermi sheet with the $\Gamma - X$ path is marked as *P*, where the length of $\Gamma - P$ is close to 1/3 of $\Gamma - X$. The nesting vector of the triple CDW is marked by the grey arrow. **c**, Theoretical band structure of the *ab*-plane monolayer along the high symmetry lines. The five colored bands are divided by their components shown in Supplementary Fig. 9. The purple and blue bands are mostly contributed by *p* orbitals of top and bottom layer Te atoms. The coral, dark green and light green bands are mostly contributed by *p* orbitals of middle layer Te atoms. The two black arrows mark the high density of states near the Fermi level at 1/3 $\Gamma - X$ and near *Y*. Four bands (the purple, blue, dark green and light green bands) disperse weakly along the Γ -*X* direction and show apparent dispersion along the Γ -*Y* direction, while the coral band is more dispersive along the Γ -*X* direction than the Γ -*Y* direction. **d**, Constant energy intensity plots with respect to Fermi level obtained by ARPES. Two high symmetry lines are marked by black dotted lines. **e**, Integrated intensity plot with $E_F \pm 40$ meV. The large elliptical FS indicated by red dashed lines serves as a guide to the eye. **f**, 2D intensity plots measured along $\bar{\Gamma}_2 - \bar{X} - \bar{\Gamma}_1$ at $T = 30$ K and $T = 155$ K, respectively. **g**, Same as (f) but along $\bar{Y} - \bar{\Gamma}_1 - \bar{Y}$. **h**, The symmetrized energy distribution curves at k_F along the $\bar{\Gamma}_2 - \bar{X} - \bar{\Gamma}_1$ and $\bar{Y} - \bar{\Gamma}_1 - \bar{Y}$ directions, respectively.

The inter-cube Te-Te CLQBs are mostly contributed by the hybridizations of *p* orbitals of Te atoms, as shown in Fig. 1c, 1d and Fig. 3a. It is also noted that the five bands near the E_F are primarily comprised of the *p* orbitals of Te atoms, as shown in the projected energy bands

in Supplementary Fig. 9. Wavefunction norms of the five bands shown in Supplementary Fig. 9 further reveal that the inter-cube Te-Te hopping along the a -axis is much stronger than that along the b -axis, which implies that each chain along the a -axis can be regarded as one site in the 1D FS nesting model (Supplementary Fig. 8a), and a quasi-1D CDW²⁷⁻²⁹ tend to form along the b -axis. The coral band crosses the Fermi level at $1/3 \Gamma - X$ point and forms a small gap of 61 meV with the blue band around the $1/3 \Gamma - X$ point, which implies that the transition of electrons can easily take place between the two close energy bands. This electron transition could enhance the electron-phonon coupling effect, which also could contribute the formation of the triple CDW. The four bands (purple, blue, dark green and light green) show apparent dispersion along the Γ -Y direction, while a flat coral band part exists near the Y point around the Fermi level. Another kind of symmetry breaking could occur along the a -axis to reduce the high density of states near the Y point.

The DFT revealed electronic structures were experimentally verified using ARPES measurements. Figure 3d shows constant-energy plots from E_F to 0.5 eV below E_F at T=30K. It shows two converged points in the density map acquired at -0.5 eV, which represent the $\bar{\Gamma}$ points at the band bottom of two adjacent BZs according the DFT bandstructures. Determination of the $\bar{\Gamma}$ point position further allows to derive the positions of high symmetry lines $\bar{\Gamma} - \bar{Y}$ and $\bar{\Gamma} - \bar{X}$ and the BZ boundary. Figure 3e plots the intensity map at E_F where the BZ boundary is highlighted using red solid lines. The large elliptical Fermi surface with a long axis perpendicular to $\Gamma - X$ direction and the relatively flat Fermi sheets along $\Gamma - X$ direction were clearly resolved, which is in good agreement with the calculated FS in Fig. 3b. For these nearly parallel Fermi surface sheets, their high density of states along $\Gamma - X$ direction implies the formation of CDW (the translation symmetry breaking) along b -axis in real space through the potential Fermi surface nesting and/or possibly the electron-phonon coupling effect.

To clarify the triple CDW gap of ATS, the band dispersion measurements were performed at the temperatures of T=30K and 155K. Two cuts along high symmetry lines $\bar{\Gamma}_1 - \bar{X} - \bar{\Gamma}_2$ and $\bar{Y} - \bar{\Gamma}_1 - \bar{Y}$ and are presented in Fig. 3f and 3g, respectively. In Fig. 3f, the dispersive band crosses the Fermi level near $1/3 \bar{\Gamma} - \bar{X}$ at T=155K, and opens a gap at T=30K. In Fig. 3g, the dispersive band crosses the Fermi level near \bar{Y} point at T=155K, and opens a gap at

30K. The gap opening due to the triple CDW were further clearly illustrated by the symmetrized EDC cuts, as shown in Fig. 3h. The gap size is determined at \sim 135 meV (at T=30K) and is comparable with the previous STS result (at T=9K).

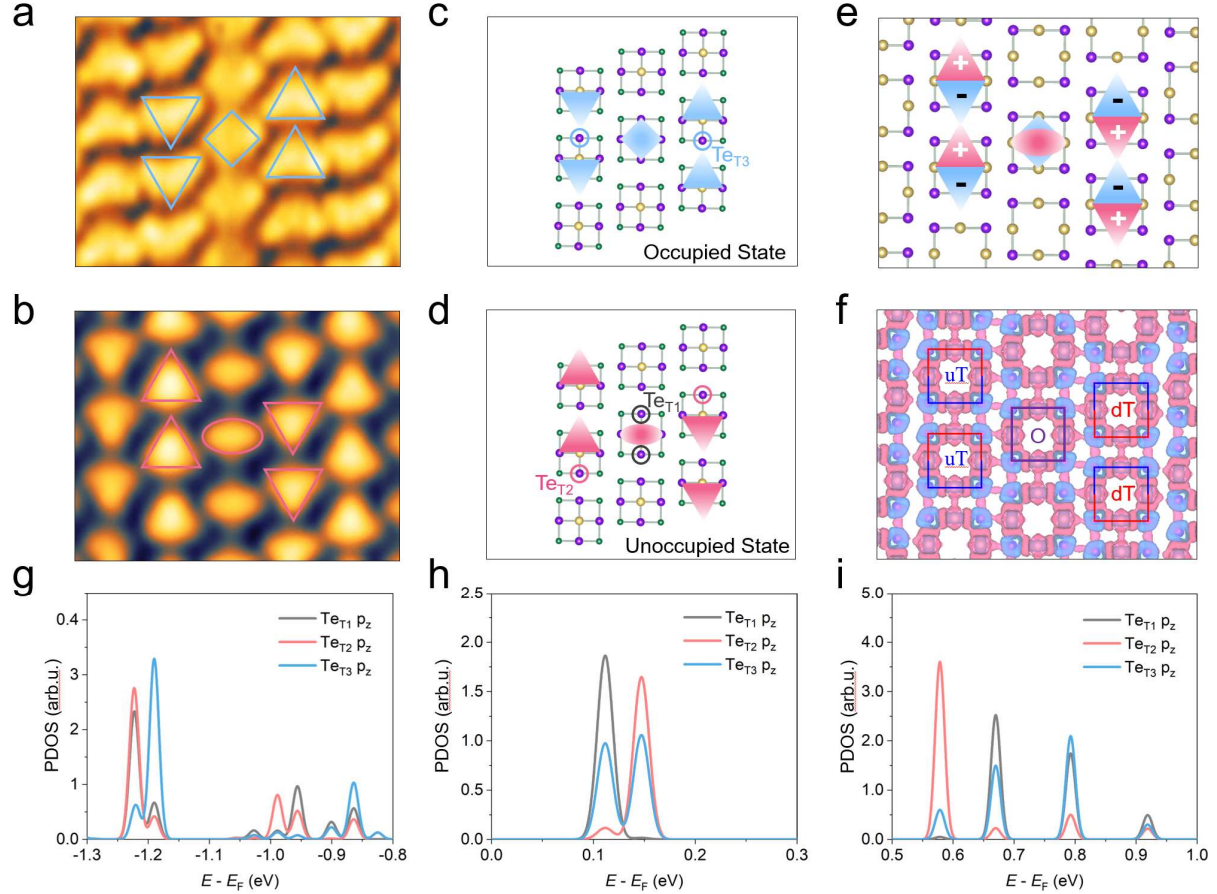


Figure 4. The polarization charge order state of ATS. **a, b** STM topography of the charge distributions within the cubes at empty states (**a**) and at occupied states (**b**), respectively. **c**, The antibonding-like and **d**, bonding-like superorbitals of the (B-A-B') tricube, corresponding to the empty state above E_F and the occupied state below E_F . **e**, The polarization charge order state of the monolayer ATS in the triple stripe charge orders. **f**, The interatomic differential charge density (DCD) of the monolayer ATS, in which the red (blue) component indicates charge accumulation (depletion). **g-i**, Projected density of states (PDOS) of p_z orbitals of Te atoms in top layer, which mostly contribute the polarization charge order states observed in the STM images. The three kinds of Te atoms are marked in the (B-A-B') tricube of (**c**). The splitting of p_z orbitals of Te_{T2} and Te_{T3} can be clearly observed in three different energy ranges (including energy splitting and state density splitting). STM size and bias voltage: scale bar 2nm, $V_s = +1.2V$ (**a**), scale bar 2nm, $V_s = -1.2V$ (**b**).

Locked electrical polarization

Our STM measurements also clearly resolved electrical polarization within individual cubes, which is relevant with the breaking degeneracy of inter-cubic Te...Te interactions and reduced the joint-DOS near the Y point (Fig. 3b and 3c). Figure 4a and 4b show high-resolution STM images of the empty and filled states of the same area, respectively, which explicitly show the uT, O and dT shaped chains. It is remarkable that the polarization directions of triangular chains are opposite in the empty and filled state images, while no polarization occurs in the cubes of O chains. These specific charge distributions within the (uT-O-dT) tri-cubes could be understood in an inter-cube hybridization picture, as illustrated in Fig. 4c and 4d.

The top or bottom slab of the ATS super-atom contains four Te atoms forming a diamond shaped electronic state. The states originated from the top and bottom slab are degenerate if no external perturbation applied, but they tend to lift the degeneration in the presence of anisotropic inter-cubic interactions. In terms of

Figure 4c and 4d show the molecular-like bonding and antibonding characteristics originating from the super-atom orbital hybridization of (B-A-B') cubes through the enhanced Te-Te bonding (highlighted by dashed ellipses), respectively. The empty state is the antibonding orbital, and the two nodal planes can be clearly observed and highlighted by the dashed lines in Fig. 4c. The occupied state is the bonding orbital, where the density of states was centrally accumulated, as shown in Fig. 4d.

As shown in Fig. 4e, the exotic antipolar electronic states along the *a*-axis formed through the translation symmetry breaking along the *b*-axis (tripe CDW) in the low-symmetric triclinic intercube Te-Te CLQB. For the tricube (B-A-B') supercell, the inversion symmetry of B (and B') cube is lost, while the inversion-symmetry of A cube is still preserved. Electronic dipole formed due to the charge polarization within the B (and B') cube along the *a*-axis. The dipoles are parallel alignment within the B (and B') columns, but antiparallel alignment between the B and B' columns (Supplementary Fig. 10). Fig. 4f shows the calculated interatomic differential charge density (DCD) of the monolayer ATS in the triple stripe charge orders. Accompanying with the formation of the triple stripe charge order, cube B and B' slightly slide toward the

central cube A along the *a*-axis, resulting in the enhanced intercube orbital hybridizations (highlighted by dashed ellipses) of A-B and A-B'.

The triple CDW (along the *b*-axis) and charge polarization (along the *a*-axis) correlatedly constitute the experimentally observed triple stripe charge order, manifesting as a unique antipolar electronic states realized in the supercrystal of ATS. The charge polarization within the cube (along the *a*-axis) originate from the inversion symmetry breaking to reduce the high DOS near the Y point, while the specific polarization configurations are selectively determined by the triple CDW charge order (along the *b*-axis).

Discussion

The exotic polarization metallic states were firstly predicted by P. W. Anderson and E. I. Blount in 1965³⁰. Until now, roughly 40 kinds of polar metallic materials have been theoretically predicted³¹, while only very few have been discovered and confirmed in experiments^{32,33}. At here, the antipolar metallic states are firstly discovered, which will inspire more theoretical and experimental work in this field.

The breaking of inversion symmetry (along the *a*-axis) on B and B' cubes are displayed by their triangular electronic states in the STM images, which are mainly contributed by the Te atoms of top layer (as shown in Supplementary Fig. 6). The Te atoms (along the *a*-axis) on the top layer can be divided into three categories: Te_{T1} (on A), Te_{T2} and Te_{T3} (on B and B') (see Fig. 4c). Fig. 4g-i shows the projected density of states (PDOS) of the *p*_z orbitals of the three Te atoms. The breaking of inversion symmetry on B and B' cubes is clarified by the relative energy shifting and intensity differentiation of the peaks in the PDOS of Te_{T2} and Te_{T3}, which confirmed the polarization inside cube B and B'.

In summary, we reported an in-depth investigation of the emerged triple stripe charge order in the layered super-atomic crystal of ATS by a combination of experimental STM/STS, ARPES, transport and Raman measurements and theoretical calculations. The triple stripe charge order consists of two sequential-emerged anisotropic CDW and antipolar charge orders.

The CDW charge modulation is attributed to the quasi-1D Fermi surface nesting along the *b*-axis, while the antipolar state originate from the spontaneous polarizations (inversion symmetry-breaking) of super-atomic cubes along the-*a* axis and their selective coupling with the translation symmetry-breaking of CDW via the low-symmetric crystal geometric structure (Supplementary Fig. 11). Given the high and precise tunability of super-atomic crystals, this work will inspire future efforts aimed at understanding and exploiting of emerged novel electronic states and properties in tailoring their super-atomic building blocks and strong non-covalent interactions among them.

Reference:

1. Kamihara, Y., Watanabe, T., Hirano, M. & Hosono, H. Iron-based layered superconductor $\text{La}[\text{O}_{1-x}\text{F}_x]\text{FeAs}$ ($x = 0.05\text{-}0.12$) with $T_c=26$ K. *J. Am. Chem. Soc.* **130**, 3296-3297, (2008).
2. Liu, Y. et al. Correlating crystallographic orientation and ferroic properties of twin domains in metal halide perovskites. *ACS Nano* **15**, 7139-7148, (2021).
3. Huang, H. et al. Growth mechanism of strongly emitting $\text{CH}_3\text{NH}_3\text{PbBr}_3$ perovskite nanocrystals with a tunable bandgap. *Nat. Commun.* **8**, 996, (2017).
4. Shengwei Jiang., Jie Shan., & Kin Fai Mak. Electric-field switching of two-dimensional van der Waals magnets. *Nat. Mater.* **17**, 406-410, (2018).
5. Bevin H. et al. Electrical control of 2D magnetism in bilayer CrI_3 . *Nature Nanotech.* **13**, 544-548, (2018).
6. D. R. Klein. et al. Probing magnetism in 2D van der Waals crystalline insulators via electron tunneling. *Science* **360**, 1218-1222, (2018).
7. Zhao, Y. et al. Extraordinarily strong interlayer interaction in 2D layered PtS_2 . *Adv. Mater.* **28**, 2399-2407, (2016).
8. Qiao, J. et al. Few-layer tellurium: one-dimensional-like layered elementary semiconductor with striking physical properties. *Sci. Bull.* **63**, 159-168, (2018).
9. Zhao, Y. et al. High-electron-mobility and air-stable 2D layered PtSe_2 FETs. *Adv. Mater.* **29**, 1604230, (2017).
10. Zhao, Y. et al. Extraordinarily strong interlayer interaction in 2D Layered PtS_2 . *Adv. Mater.* **28**, 2399-2407, (2016).
11. Evan, A. D. et al. Superatoms in materials science. *Nat. Rev. Mater.* **5**, 371-387, (2020).
12. Wei H. et al. Two-dimensional inorganic molecular crystals. *Nat. Commun.* **10**, 4728, (2019).
13. Voevodin, A., Campos, L. M. & Roy, X. Multifunctional vesicles from a self-assembled cluster-containing diblock copolymer. *J. Am. Chem. Soc.* **140**, 5607-5611, (2018).
14. Cui, X. et al. Realizing nearly-free-electron like conduction band in a molecular film through mediating intermolecular van der Waals interactions. *Nat. Commun.* **10**, 3374, (2019).
15. Li, G. et al. Self-assembly of C_{60} monolayer on epitaxially grown, nanostructured graphene on Ru(0001) surface. *Appl. Phys. Lett.* **100**, 013304, (2012).
16. Anderson, P. W. The resonating valence bond state in La_2CuO_4 and superconductivity. *Science* **235**, 1196-1198, (1987).
17. Guo, J. et al. Superconductivity in the iron selenide $\text{K}_x\text{Fe}_2\text{Se}_2$ ($0 < x < 1.0$). *Phys. Rev. B* **82**, 180520(R), (2010).

18. Ang, R. et al. Real-space coexistence of the melted mott state and superconductivity in Fe-substituted 1T-TaS₂. *Phys. Rev. Lett.* **109**, 176403, (2012).
19. Cai, X. et al. Atomically thin CrCl₃: an in-plane layered antiferromagnetic insulator. *Nano Lett.* **19**, 3993-3998, (2019).
20. Fang, A. et al. STM studies of TbTe₃: evidence for a fully incommensurate charge density wave. *Phys. Rev. Lett.* **99**, 046401, (2007).
21. Malliakas, C. et al. Square nets of tellurium: rare-earth dependent variation in the charge-density wave of ReTe₃ (RE) rare-earth element). *J. Am. Chem. Soc.* **127**, 6510-6511, (2005).
22. Denholme, S. J. et al. Coexistence of superconductivity and charge-density wave in the quasi-one-dimensional material HfTe₃. *Sci. Rep.* **7**, 45217, (2017).
23. Tang, F. D. et al. Three-dimensional quantum Hall effect and metal–insulator transition in ZrTe₅. *Nature*. **569**, 537-541, (2019).
24. Schutte, W. J. & De Boer, J. L. Valence fluctuations in the incommensurately modulated structure of calaverite AuTe₂. *Acta Cryst.* **B44**, 486-494, (1988).
25. Guo, J.G. et al. Quasi-two-dimensional superconductivity from dimerization of atomically ordered AuTe₂Se_{4/3} cubes. *Nat. Comm.* **8**, 871, (2017).
26. Jia, X. Yu. et al. Nodeless superconductivity in a quasi-two-dimensional superconductor AuTe₂Se_{4/3}. *Chin. Phys. B.* **27**, 067401, (2018).
27. Zhua, X., Guo, J., Zhang, J. & Plummer, E. W. Misconceptions associated with the origin of charge density waves. *Adv Phys.* **2**, 622–640, (2017).
28. Gruner, G. in *Density waves in solids*, vol. 89, (Addison-Wesley Publishing Company, Massachusetts, 1994).
29. Peierls, R.E. in *Quantum theory of solids*, (Oxford University, New York, 1955).
30. Anderson, P. W. & Blount, E. I. et al. Symmetry considerations on martensitic transformations: "ferroelectric" metals? *Phys. Rev. Lett.* **14**, 532 (1965).
31. Zhou, W. X. & Ariando. A. Review on ferroelectric/polar metals. *Jpn. J. Appl. Phys.* **59**, SI0802 (2020).
32. Fei, Z. Y. et al. Ferroelectric switching of a two-dimensional metal. *Nature*. **560**, 336–339 (2018).
33. Sharma, P. et al. A room-temperature ferroelectric semimetal. *Sci. Adv.* **5**, eaax5080, (2019).

Materials and Methods

Sample preparation and STM measurements. Single crystals of AuTe₂Se_{4/3} were grown by the self-flux method. They are in shape of small platelets with shining mirror-like surfaces, typically 2×8×0.2 mm³. The samples were cleaved in ultrahigh vacuum at room temperature, and subsequently cooled down for STM measurements. STM experiments were performed in a commercial variable-temperature STM (PanScan Freedom, RHK) operated in ultrahigh vacuum. Electrochemically etched polycrystalline tungsten calibrated on clean Au(111) surfaces were used for all our STM measurements tips. The STM topography was taken in the constant-current mode, and the dI/dV spectra were collected using a standard lock-in technique with a modulation frequency of 999.1 Hz. The STM measurements was performed mostly at 9 K for the high-resolution imaging, and at variable temperatures (from 9K to Room Temperature) for the phase transition characterization.

XRD, SEM and transport measurements: The powder X-ray diffraction (PXRD) pattern of polycrystalline AuTe₂Se_{4/3} were measured by panalytical X'pert diffractometer with Cu-K α anode ($\lambda = 1.5408$ Å). The scanning electron microscopy (SEM) image of single crystal was captured from Hitachi S-4800 FE-SEM.

The electrical resistivity (ρ) was measured through the standard four-wire method at PPMS (Quantum Design).

Raman measurements: Raman spectroscopy were performed on a home-built Raman system equipped with a semiconductor laser ($\lambda=532$ nm), a $100\times$ objective (numerical aperture 0.9) and a 600 lines mm^{-1} grating. To prevent the CDW phase transition driven by laser irradiation, the laser irradiance was kept below $100 \mu\text{W}/\mu\text{m}^2$. The sample was placed into a liquid-helium cryostat (attocube systems AG, Germany) with a heater to control the temperature. The step size of Raman mapping was $1 \mu\text{m}$. All the peaks were calibrated with the Si peak at 520.7 cm^{-1} .

ARPES measurements: ARPES measurements were performed at Renmin University of China equipped with a Scienta DA30 analyzer, with photon energy of 10.05 eV, and the BL13U beamline of National Synchrotron Radiation Laboratory (NSRL) equipped with a Scienta R4000 analyzer. The energy and angular resolution were set to 10 meV and 0.3° , respectively. Clean surfaces for ARPES measurements were obtained by *in situ* cleaving the samples. Photoemission spectra presented in this work were recorded at $T=30$ K and 155 K using the photo energy from 21 to 45 eV, in a working ultrahigh vacuum better than 6×10^{-11} Torr.

Theoretical calculations. Density functional theory calculations were performed using the generalized gradient approximation for the exchange-correlation potential, the projector augmented wave method^{34,35}, and a plane-wave basis set as implemented in the Vienna *ab-initio* simulation package (VASP)³⁶. Dispersion corrections were made at the van der Waals density functional (vdW-DF) level^{37,38}, with the optB86b functional for the exchange potential (optB86b-vdW)^{39,40}. The kinetic energy cut-off for the plane-wave basis was set to 700 eV for the geometric properties of monolayer $\text{AuTe}_2\text{Se}_{4/3}$ and 350 eV for electronic structure calculations. A $7\times 7\times 1$ k -mesh was used to sample the first Brillouin zone in the unit cell and a denser k -mesh of $20\times 20\times 1$ is utilized to plot the Fermi surface. A k -mesh of $2\times 7\times 1$ was adopted for structure optimization and electronic structure calculations in 3×1 supercell. A vacuum layer of around 17 Å was used to model monolayered structures. The shape and volume of the unit cell and the 3×1 supercell of $\text{AuTe}_2\text{Se}_{4/3}$ were fully relaxed until the residual force per atom was less than $0.01 \text{ eV}/\text{\AA}$. A method of Methfessel-Paxton with sigma of 0.05 eV and a tetrahedron method with sigma of 0.05 eV were used for geometric properties optimization and charge density calculations, respectively. PDOSs of the 3×1 supercell were calculated with a Gaussian smearing with sigma of 0.01 eV. In band structure calculation, 121 points are equally set along the $\text{X}-\Gamma-\text{Y}-\text{H}_1$ path in the reciprocal space. A non-selfconsistent calculation for a superposition of atomic charge density (ρ_{nscf}) was calculated and subtracted from selfconsistently calculated atomic charge density (ρ_{scf}) in the 3×1 supercell to get the atomic differential charge, *i.e.*, $\rho_{\text{DCD}} = \rho_{\text{scf}} - \rho_{\text{nscf}}$.

Reference:

34. Blöchl, P. E. Projector augmented-wave method. *Phys. Rev. B* **50**, 17953 (1994).
35. Kresse, G. & Joubert, D. From ultrasoft pseudopotentials to the projector augmented-wave method. *Phys. Rev. B* **59**, 1758 (1999).
36. Kresse, G. & Furthmüller, J. Efficient iterative schemes for ab initio total-energy calculations using a plane-wave basis set. *Phys. Rev. B* **54**, 11169 (1996).
37. Dion, M., Rydberg, H., Schröder, E., Langreth, D. C. & Lundqvist, B. I. Van der Waals density functional for general. *Phys. Rev. Lett.* **92**, 246401 (2004).
38. Lee, K., Murray, É. D., Kong, L., Lundqvist, B. I. & Langreth, D. C. Higher-accuracy van der Waals density functional. *Phys. Rev. B* **82**, 081101 (2010).

39. Klimeš, J., Bowler, D. R., & Michaelides, A., Van der Waals density functionals applied to solids. *Phys. Rev. B* **83**, 195131 (2011).
40. J. Klimeš., Bowler, D. R. & . Michaelides, A. Chemical accuracy for the van der Waals density functional. *J. Phys. Condens. Matter* **22**, 022201 (2009).

Acknowledgments

This project is supported by the National Natural Science Foundation of China (NSFC) (No. 61674045, 11604063, 61911540074, 51922105), the Ministry of Science and Technology (MOST) of China (No. 2016YFA0200700), the Strategic Priority Research Program (Chinese Academy of Sciences, CAS) (No. XDB30000000). Z.H.Cheng was supported by the Fundamental Research Funds for the Central Universities and the Research Funds of Renmin University of China (No. 21XNLG27).

Author contributions

S. X. and Z. C. conceived research idea and plan. S. X. performed the STM experiments and analysis of STM data. Z. W. and S. W. S. X. performed the ARPES experiments and analysis of ARPES data. X. C. and J. G and X. L. C. grew the single crystals. X. C. performed transport, SEM and XRD measurements. H. L. and L. X. and S. H. performed Raman measurements. L. W. and W. J. performed the DFT calculations. S. X. and Z. C. prepared the manuscript. All authors discussed the results and contributed to the manuscripts.